



HAL
open science

Assessing the ability of the 2D Fisher-KPP equation to model cell-sheet wound closure

Abderrahmane Habbal, H el ene Barelli, Gr egoire Malandain

► **To cite this version:**

Abderrahmane Habbal, H el ene Barelli, Gr egoire Malandain. Assessing the ability of the 2D Fisher-KPP equation to model cell-sheet wound closure. *Mathematical Biosciences*, 2014, 252, pp.45-59. hal-00923588

HAL Id: hal-00923588

<https://inria.hal.science/hal-00923588>

Submitted on 3 Jan 2014

HAL is a multi-disciplinary open access archive for the deposit and dissemination of scientific research documents, whether they are published or not. The documents may come from teaching and research institutions in France or abroad, or from public or private research centers.

L'archive ouverte pluridisciplinaire **HAL**, est destin ee au d ep ot et  a la diffusion de documents scientifiques de niveau recherche, publi es ou non,  emanant des  tablissements d'enseignement et de recherche fran ais ou  trangers, des laboratoires publics ou priv es.

Assessing the ability of the 2D Fisher-KPP equation to model cell-sheet wound closure

Abderrahmane Habbal^{a,*}, Hélène Barelli^b, Grégoire Malandain^c

^aUniv. Nice Sophia Antipolis, CNRS, LJAD, UMR 7351, Parc Valrose, 06108 Nice, France

^bUniv. Nice Sophia Antipolis, CNRS, IPMC, UMR 7275, 06560 Sophia Antipolis, France

^cINRIA, 2004 route des Lucioles, 06900 Sophia Antipolis, France

Abstract

We address in this paper the ability of the Fisher-KPP equations to render some of the dynamical features of epithelial cell-sheets during wound closure.

Our approach is based on nonlinear parameter identification, in a two-dimensional setting, and using advanced 2D image processing of the video acquired sequences. As original contribution, we lead a detailed study of the profiles of the classically used cost functions, and we address the "wound constant speed" assumption, showing that it should be handled with care.

We study five MDCK cell monolayer assays in a reference, activated and inhibited migration conditions. Modulo the inherent variability of biological assays, we show that in the assay where migration is not exogeneously activated or inhibited, the wound velocity is constant. The Fisher-KPP equation is able to accurately predict, until the final closure of the wound, the evolution of the wound area, the mean velocity of the cell front, and the time at which the closure occurred. We also show that for activated as well as for inhibited migration assays, many of the cell-sheet dynamics cannot be well captured by the Fisher-KPP model. Finally, we draw some conclusions related to the identified model parameters, and possible utilization of the model.

Keywords: MDCK, cell-sheet, Fisher-KPP, 2D simulation, image processing, wound edge dynamics.

*Corresponding author: habbal@unice.fr

Contents

1	Introduction	2
2	Methodology	5
2.1	Experimental methodology	5
2.2	Mathematical methodology	6
3	Preliminary analysis	10
3.1	Experimental and computed variables	11
3.2	Profile of the cost functions	12
4	Results	13
4.1	Wound closure occurs	13
4.2	Wound closure fails	20
5	Conclusion	25

1. Introduction

Morphogenesis, embryogenesis and wound healing processes involve complex movements of epithelial cell sheets. As well, more than 90% of malignant tumors in adult mammals occur in epithelial tissues. The growth, aggressiveness and lethality of these carcinomas is intimately related to the machinery of the collective cell migration and proliferation triggered in epithelial lines.

Migration and proliferation of epithelial cell sheets are the two keystones underlying the collective cell dynamics in these biological processes. It is then of utmost importance to understand their underlying mechanisms.

The cells in epithelial sheets (a.k.a. monolayers) maintain strong cell-cell contact during their collective migration. Although it is well known that under some experimental conditions apical and basal sites play distinctive important roles during the migration, as well as the substrate itself [1], we consider here assays where the apico-basal polarization does not take place. Thus, the cell monolayer can be considered as a 2 dimensional continuous structure. These epithelial monolayers, among which are the Madin-Darby Canin Kidney (MDCK) cells [2, 3] are universally used as multicellular models to study the migratory mechanisms, most of them being triggered by scratching with a pipette cone or blades during *wound healing* assays.

Immediately after a wound is created in an MDCK monolayer plate, the cells start to move in order to fill in the empty space. This movement, the wound closure, is a highly-coordinated collective behavior yielding a structured cohesive front, the wound leading edge.

The wound closure involves biochemical processes and mechanical forces, still far from being well understood, which are distributed *over the whole monolayer* [4, 1].

They also strongly depend on the specific geometrical constraints of the cells environment [5]. Regardless of these complex processes, much particular attention was paid to the specific study of the movement of the leading edge.

In most cases, wound edge-specific quantitative studies amount to the determination, under different assay conditions, of the rate of migration and averaged velocity of the cells located on the wound front. The assay conditions generally intend to study the impact of migration activators like the Hepatocyte Growth Factor (HGF) [6, 7] or inhibitors like phosphoinositide 3-kinase (PI3K) inhibitors. HGF, also known as scatter factor (SF), is a mesenchymal-derived or stromal-derived multifunctional growth factor with motogenic, and morphogenic activities. HGF plays an important role in the development and progression of cancer. Particularly, HGF promotes tumor metastasis by stimulating motility and invasion [8]. HGF enhances cell migration and HGF-induced migration depends on PI3K/Akt signaling pathway [9]. The activation of PI3K/Akt pathway induced by HGF is involved in the downregulation of cell adhesion molecules and in changes in actin organisation, contributing to the attenuation of cell-cell adhesion and promoting the enhanced motility and migration of epithelial or melanoma cells [10, 11]. LY294002, a PI3K inhibitor, is able to inhibit HGF-induced cell migration.

Here, in our assays, we used HGF and LY 294002, among hundreds of proteins which directly or by mediation influence cell migration. HGF is able to induce motility and cellular rearrangements within a confluent monolayer without compromising the paracellular barrier function. This property may be particularly pertinent to processes such as wound healing in tissues [14]. It allows to consider the monolayer even in stimulated condition as a single entity because all the cells stay interconnected.

The recourse to validated mathematical models dedicated to the simulation of wound edge dynamics may be a twofold benefit to the biologists: save experimental trials, and get access to hidden parameters (while keeping in mind the limits of the validity of the model). Validated models may be used to perform sophisticated (i.e. may reveal more discriminating) classification of migration-related proteins through the classification of the model-dependent calibrated parameters [15].

Epithelial cell-sheet movement is complex enough to undermine most of the mathematical approaches based on *locality*, that is mainly traveling wavefront-like partial differential equations. In [16] it is shown that MDCK cells extend cryptic lamellipodia to drive the migration, several rows behind the wound edge. In [17] MDCK monolayers are shown to exhibit similar non local behavior (long range velocity fields, very active border-localized leader cells).

Nonetheless, we presently address one of these approaches, stressing its abilities and failures in faithfully predicting at least in a kinematic viewpoint the cell-sheet movement. We have selected one of the simplest models, the Fisher-KPP equation detailed in the section 2.2, amongst the general family of semilinear reaction-diffusion equations. These are widely used to set a phenomenological description of the time and spatial changes occurring within cell populations that undergo scattering (moving), spreading (expanding cell surface) and proliferation, three of the most important mechanisms during the wound closure. The reaction-diffusion equations, coupled to

visco-elasticity mechanics, may account as well for chemotaxis and haptotaxis among other cell movement characteristics, see e.g. [18, 19, 20, 21]. Of course, there are many mathematical models other than the reaction-diffusion ones, e.g. in [22] where the MDCK cell-sheet is considered as a visco-elastic medium. In [23], the authors derive a continuum approximation for a one dimensional individual-based model which describes a system of adherent cells. A particle-based with stochastic motion model is studied in [24], and in [25] the authors investigate the minimal requirements needed for the emergence of a collective behavior of epithelial cells, highlighting the role of cell motility and cell-cell mechanical interactions.

To our knowledge, the first works investigating the validity of one dimensional-Fisher-KPP equation to model the wound edge velocity of cell-sheets are [26] and [27]. In [28] the cell-sheet is modeled as a two-dimensional compressible fluid flow, physical assumptions made therein amount to consider a final equation, which turns out to be of Fisher-KPP type, with free boundary formulation. Similar to our methodology, the authors lead an optimization routine, to perform the calibration of the model dependent parameters. In [29] the authors develop a multiscale (at population and cell levels) approach, where they consider a Fisher-KPP equation with a nonlinear density-dependent diffusion, to take into account the contact inhibition effect. They proved that at the cell level the contact inhibition model was able to capture experimentally observed differences in the behavior of cells located at front and cells behind it, while the Fisher-KPP equation with constant diffusion is unable to do so. Close to our methodology, in the paper [30], image processing and Fisher-KPP model were used to quantify the migration and proliferation of skeletal cell types including MG63 and human bone marrow stromal cells (HBMSCs). The authors showed that the Fisher-KPP equation is appropriate for describing the migration behaviour of the HBMSC population, while for the MG63 cells a sharp front model is more appropriate. In [31], the authors use a lattice-based discrete model and the Fisher-KPP model, for a circular barrier assay. They obtain independent estimates of the random motility parameter and the intrinsic proliferation rate. The authors investigate how the relative roles of motility and proliferation affect the cell spreading.

Briefly speaking, our methodology is as follows. Image processing of video sequences of a given biological assay yields a specific sequence of segmented binarized wound front images. We use a subset of these sequences to identify the Fisher-KPP model parameters. The identified are then used to assess the prediction power of the mathematical model, by comparing, on a different (complementary) subset of images, the computed (predicted) sequences to the biological ones.

The paper is organized as follows. In section-2, we outline the experimental and mathematical methodologies. First, the cell-sheet assays are briefly described. Then, we introduce the used image processing procedure, Fisher-KPP equations and model calibration, *id est* identification by optimization techniques of the diffusion parameter D and proliferation rate r . Then, important computational issues are addressed in section-3, among which is the study of the profiles of cost functions.

The optimization approach, the image processing algorithms and the detailed study of the cost functions profiles, as well as the stressing of the popular use of the assump-

tion ” wound velocity = $2\sqrt{rD}$ ” form, to our knowledge, an original contribution.

In order to assess the validity of the Fisher-KPP model, we consider five MDCK assays in section-4. In a first part, three qualitatively different assays which lead the wound to closure are studied. In the second part, the model calibration is performed for two assays which fail to close due to the addition of migration inhibitors. Finally, a concluding section-5 discusses the validity limits of the mathematical model and its ”notwithstanding” usefulness.

2. Methodology

2.1. Experimental methodology

We first shortly describe the conditions for the biological assays, then we detail the main steps of the used image processing techniques.

The cell-sheet assays

MDCK cells were plated on plastic dishes coated with collagen I at 3 $\mu\text{g}/\text{ml}$ to form monolayers. Confluent monolayers were wounded by scraping with a tip, rinsed with media to remove dislodged cells, and placed back into MEM (Minimum Essential Medium) with 5% FBS (Fetal Bovine Serum). Cell sheet migration into the cleared wound area (the notch is 350 μm width by 22 mm length) was recorded using a Zeiss Axiovert 200M inverted microscope equipped with a thermostated incubation chamber maintained at 37 $^{\circ}\text{C}$ under 5% CO_2 . Digital images were acquired every 2 min for 12 h using a CoolSnap HQ CCD camera (Princeton, Roper Scientific). Examples of such images are presented in Figure-2(a).

Five different assays were recorded, yielding five data sets, composed each of 360 images. From each data set, we extracted a sequence of 120 2D images of 1392×1040 pixels (a pixel size represents $0.645 \times 0.645 \mu\text{m}^2$), encoded on 2 bytes, corresponding to a time step of 6 min between 2 consecutive images.

The assays are classified as follows:

- Assay-I: control conditions
- Assay-II and Assay-III control conditions + HGF (Hepatocyte Growth Factor)
- Assay-IV and Assay-V control conditions + inhibitor

By putting all the images of the sequence into a stack, we obtained a 3D image, with two spatial dimensions (X and Y), the third one, T , being temporal (the voxel thickness is of 6 min). It is then possible to extract XT cross-sections, or kymographs, (as presented in Figure-6(f)) that allows to visually assess the dynamics of the wound edge (compare for instance Figures 6(f), 11(f), and 13(f)).

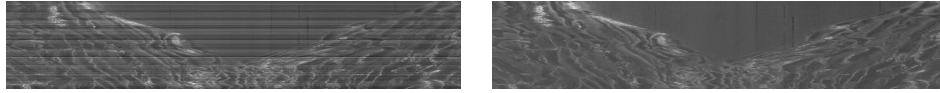


Figure 1: Left, original stack exhibiting illumination inhomogeneities across 2D images. Right, after intensity homogenization.

If necessary, intensity inhomogeneities between images (see Figure-1) are corrected with the approach described in [32].

We next give a few details on the main image processing tasks, which yield the experimental wound edge speed values, as well as usable (for computational needs) binarized monolayer sequences.

Wound edge detection

To quantify the propagation speed of the wound edge, we first detect the latter in the images. To that end, we use the following operations, illustrated by Figure-2.

1. We enhance both the cell walls and nuclei. We use first a top-hat operator: this mathematical morphology [33] operation is the difference between the image and its opening (with a 2D disk of radius 30 pixels as structuring element), and enhances the cell walls (Figure-2(b)). A conjugated top-hat operator (difference between the closing and the image (with a 2D disk of radius 20 as structuring element) is also performed on the original image to enhance the cell nuclei (Figure-2(c)). The maximum value of the two operations yields the final enhanced image (Figure-2(d)).
2. Each section is thresholded: the same threshold, chosen by the user, is used for all the sections of a sequence (Figure-2(e)).
3. At this stage, each slice has been processed independently. To add some coherency from slice to slice, we process the whole stack as a 3D volume, and we perform a morphological opening (Figure-2(f)) followed by a morphological closing (Figure-2(g)), both with a 6-neighborhood [34], which is a 3D structure, as a structuring element.
4. The last step consists in eliminating the smallest 4-connected components in each section, *i.e.* the ones with less than 10,000 pixels (Figure-2(h)).

2.2. *Mathematical methodology*

In the present section, we introduce the ingredients of the mathematical model, namely the Fisher-KPP equations. Then follows a short presentation of the optimization framework set for the identification (or calibration) of the model parameters.

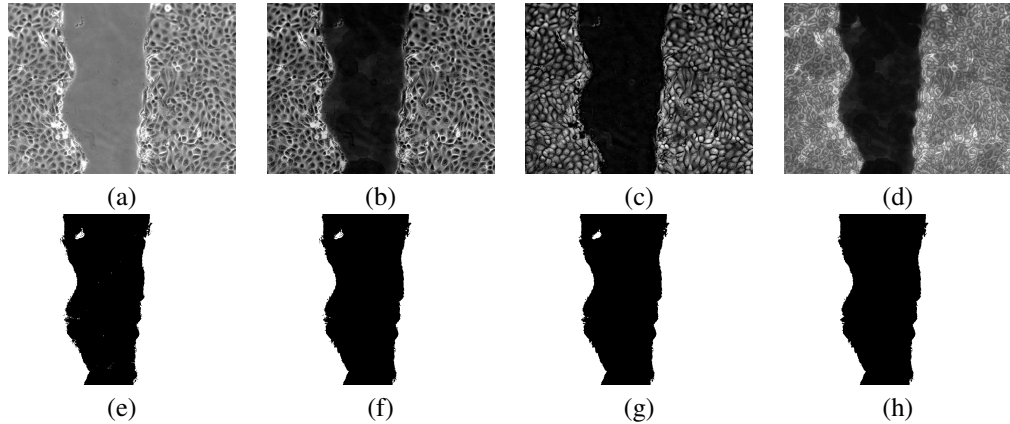


Figure 2: The different steps of the image processing pipeline. The upper left image is an original section, while the lower right one is the binarized wound front. See the text for the details.

Fisher-KPP equations

Fisher-KPP equation is a semilinear parabolic partial differential equation, introduced in 1937 by Fisher [35] and Kolmogoroff-Petrovsky-Piscounoff [36] which models the interaction of Fickian diffusion with logistic-like growth terms.

First, let us introduce the equation in its most classical presentation, before discussing its main features and relevance to model the wound healing of monolayers.

We denote by Ω a rectangular domain, typically an image frame of the monolayer, by Γ_D its vertical sides and by Γ_N its horizontal ones.

We assume that the monolayer is at confluence, and consider the cell density relatively to the confluent one. The Fisher-KPP equation then reads

$$\frac{\partial u}{\partial t} = D\Delta u + ru(1-u) \quad \text{in } \Omega \quad (1)$$

where $u = u(t, \mathbf{x}) = \frac{\text{cell density}}{\text{cell density at confluence}}$ denotes the relative cell density at time t and position $\mathbf{x} = (x, y) \in \Omega$. The parameter D is the diffusion coefficient and r is the linear growth rate. The two latter parameters are assumed constant. The operator $\Delta = \frac{\partial^2}{\partial x^2} + \frac{\partial^2}{\partial y^2}$ is the Laplace operator.

To complete the formulation of the Fisher-KPP equation, initial and boundary conditions must be specified. Classically, at $t = 0$ one has at hand an initial (binarized) monolayer image $u_0(\mathbf{x})$. Then, one simply sets:

$$u(0, \mathbf{x}) = u_0(\mathbf{x}) \quad \text{over } \Omega. \quad (2)$$

Boundary conditions are more delicate to set. If we refer to our own case-study, see the computational domain setting as sketched in Figure-3, there are always cells on the

vertical sides, so that we may set:

$$u(t, \mathbf{x}) = 1 \text{ on } \Gamma_D \quad (3)$$

and the cell flux across the horizontal sides is assumed to be negligible:

$$\frac{\partial u}{\partial n}(t, \mathbf{x}) = 0 \text{ on } \Gamma_N \quad (4)$$

where $\frac{\partial u}{\partial n}$ is the normal derivative of u .

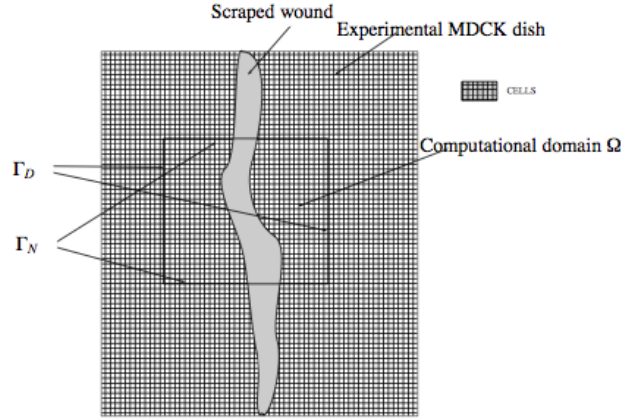


Figure 3: The computational domain Ω is a restriction of the overall scraped area. MDCK cells always show on the vertical sides of the image frame, and it is assumed that the amount of cells traveling across the horizontal ones is negligible. Dimensions of a typical dish are $350\mu\text{m}$ width by 22mm length.

This latter assumption is particularly relevant when the image is only a part of a larger scraped observation area. We then are more or less assuming a local symmetry condition, that is, the migration velocity is normal to the leading edge near the horizontal sides where the domain cutoff was performed. Although questionable, the above choice of boundary conditions proved to lead to computational experiments in good agreement with the biological observed ones.

One of the main features of the Fisher-KPP equation is that it drives initial stiff fronts (e.g. an 1-0 Heaviside-like function) to closure, *id est* to the stable steady solution $u = 1$ everywhere, by propagating the front with a constant velocity $V_{th} = 2\sqrt{rD}$ (up to a short transition time). This mathematical feature is central in our present study.

In the following, we detail the steps of our procedure of identification of the (r, D) parameters for the Fisher-KPP equation.

Identification of the Fisher-KPP parameters

Let us denote by Ω the rectangular domain which defines the images frame, and by $[T_0, T]$ the time window used to calibrate the constant parameters r and D . This

time window is a subset of the overall acquisition duration $[0, T_F]$ where T_F is the final available observed time (in our case, $T_F = 720$ min).

In order to validate the mathematical model, it is common to use experimental data observed during the early $[T_0, T]$ time interval to identify the parameters, and then use the identified parameters to predict quantities like as wound area or velocity variations, and compare the computational results to the non exploited experimental data observed during the time interval $[T, T_F]$.

Let us denote by $(u_{exp}(t, \mathbf{x}))$ the sequence of experimental cell density images (segmented and binarized), and let be the observation-error function J defined by

$$J(r, D; v) = \int_{T_0}^T \int_{\Omega} |v(t, \mathbf{x}) - u_{exp}(t, \mathbf{x})|^2 d\mathbf{x} dt.$$

To justify the mathematical meaning of the difference $v(t, \mathbf{x}) - u_{exp}(t, \mathbf{x})$ (the first term is continuous while the second is binary), let us recall that the present study focuses on wound front dynamics. The F-KPP equation, starting with a binarized initial solution, is expected to propagate the front, showing a thin transition interface (due to the diffusion term). Thus, the continuous solution v is made of ?1? and ?0? surfaces linked by this thin interface, being almost of the same kind than the binarized u_{exp} .

The identification method is classical, it amounts to minimize, subject to specified constraints, the following cost function j :

$$j(r, D) = J(r, D; u(r, D)) \quad (5)$$

where $u(r, D)$ is the unique solution to the Fisher-KPP system (1)-(2)-(3)-(4).

The constraints are of bound type:

$$r_{min} \leq r \leq r_{max} ; \quad D_{min} \leq D \leq D_{max}$$

where the above lower and upper bounds may be e.g. estimated from experimental published data (or simply taken as the smallest and largest biophysically relevant ones).

Performing the numerical minimization of the cost j may be computationally expensive even though the space of parameters is of very small dimension, since each cost evaluation requires the numerical solution of the time-dependent Fisher-KPP semilinear partial differential equation. It is then of importance to save computational time whenever it is possible. To this end, the computation of the gradient of the cost may help to efficiently use fast gradient descent minimization algorithms, and compute accurate approximate cost functions of higher order (using e.g. Hermite polynomials) which are cheap to evaluate. It is a classical theoretical result that the cost function is differentiable with respect to (r, D) . We give hereafter the steps to rapidly compute the exact gradient of j , based on the adjoint state method, see for instance the book [37].

Let us, for instance, define the (Fisher-KPP system) adjoint state solution as the unique solution p to the retrograde linear partial differential equation:

$$-\frac{\partial p}{\partial t} = D\Delta p + r(1 - 2u)p + 2(u - u_{exp}) \quad \text{in } \Omega \quad (6)$$

with the following boundary conditions, consistent with the ones stated above for the Fisher-KPP solution u :

$$p(t, \mathbf{x}) = 0 \text{ over } \Gamma_D \quad \frac{\partial p}{\partial n}(t, \mathbf{x}) = 0 \text{ over } \Gamma_N \quad (7)$$

and with a final condition prescribed at $t = T$:

$$p(T, \mathbf{x}) = 0 \text{ in } \Omega. \quad (8)$$

The adjoint state formula yields the gradient of the cost function j :

$$\frac{\partial j}{\partial r}(r, D) = \int_{T_0}^T \int_{\Omega} u(1-u)p \, d\mathbf{x}dt, \quad (9)$$

$$\frac{\partial j}{\partial D}(r, D) = - \int_{T_0}^T \int_{\Omega} \nabla u \nabla p \, d\mathbf{x}dt. \quad (10)$$

To solve the Fisher-KPP system, we used an explicit Euler forward finite difference in time, and centered second order five points finite difference in space. The numerical scheme is convergent provided a stability condition. The latter condition is satisfied thanks to the relative small magnitude of the considered diffusion and proliferation coefficients with respect to the typical time and space steps used in the present computational experiments. Indeed, spatial step is one pixel in both directions, and time step is a fraction (tenth) of the image acquisition lapse time.

We implemented our own finite difference code to solve the Fisher-KPP equations, and used the matlab optimization (fmincon) toolbox. Let us underline that the numerical approximation of the retrograde adjoint state equation (6) requires careful treatment. In particular, because of the lack of intermediate values of u_{exp} for time steps used by the numerical scheme that are not acquisition times (time interpolation is necessary). As well, the gradient formulae (9)-(10) have to be handled carefully because of the nature of the solution u which shows a stiff profile nearby the wound edge, where the whole gradient information is concentrated.

The cost function j has a strongly non-linear implicit dependence on the parameters r and D . It is then not straightforward to draw any conclusion related to the uniqueness of the minima (which do exist in the compact set defined by the bounds). Thus, in order to perform efficient numerical optimization, it is useful if not mandatory to lead a preliminary study of the profile of the cost functions.

3. Preliminary analysis

We first list the parameters, experimentally estimated or computed, which are involved in the model validation method. Then, we lead a detailed study of the profiles of the cost functions commonly used to identify the parameters. In the final part of the present section, we address the relevance of the assumption which states that experimental wound edge velocity should be *a priori imposed* as equal to the theoretical wavefront velocity.

3.1. Experimental and computed variables

On original images, $1 \text{ pixel} = 0.416 \mu\text{m}^2 = (0.645 \mu\text{m})^2$, but due to computational restrictions on the image size, original images are down resized by a rescaling factor of 8×8 . On resized images, $1 \text{ pixel} = 8 \times 8 \times 0.416 \mu\text{m}^2$, so the leading edge velocity and diffusion parameters units must be rescaled accordingly:

- Diffusion unit: $1 \text{ pixel} \cdot \text{min}^{-1} = 1.6 \cdot 10^{-3} \text{ mm}^2 \cdot \text{h}^{-1} = 1600 \mu\text{m}^2 \cdot \text{h}^{-1}$
- Velocity unit: $1 \text{ pixel}^{1/2} \cdot \text{min}^{-1} = 309 \cdot 10^{-3} \text{ mm} \cdot \text{h}^{-1}$

The bounds for the proliferation and diffusion parameters are set as follows, for the preliminary study as well as for the main identification calculations:

$$r_{\min} = 10^{-6}, r_{\max} = 0.5 \text{ (min}^{-1}) \quad D_{\min} = 10^{-8}, D_{\max} = 0.15 \text{ (pixel} \cdot \text{min}^{-1})$$

$[\mathbf{T}_0 - \mathbf{T}]$ (increments of 6 min) is the subset of images used to calibrate the model parameters r and D ;

\mathbf{r} (min^{-1}) and \mathbf{D} (pixel/min) are the proliferation rate and diffusion coefficient;

\mathbf{J} is the optimal cost function. Otherwise specified, we used $J = J_U/w_0$ where w_0 is the initial wound area (see section 3.2 for the definition of J_U);

\mathbf{V}_{exp} (pixel^{1/2}/min) is the experimental wound closure speed defined as the slope of the linear regression w.r.t. time of the leading-edge (averaged in the i-coordinates) velocities;

\mathbf{V}_{comp} (pixel^{1/2}/min) is the computed wound closure speed defined as for V_{exp} , using the PDE model leading-edge evolution;

$\mathbf{V}_{\text{th}} = 2\sqrt{rD}$ (pixel^{1/2}/min) is the theoretical wavefront velocity of the Fisher-KPP model;

\mathbf{MR}_{exp} (pixel/min) is the experimental migration rate defined as the slope of the linear regression w.r.t. time of the experimental wound area;

$\mathbf{MR}_{\text{comp}}$ (pixel/min) is the computed migration rate defined as for MR_{exp} , using the PDE model area evolution.

Notice that, throughout the paper, the experimental and computational velocities we refer to are the horizontal components of the velocity vectors, which are approximately the components perpendicular to the wound edge. Considering an Eulerian view of the wound edge rather than a Lagrangian one, the assumption is reasonable. We do not take into account the mechanical strains that are endured by the cell rows behind the edge, so that the edge tangential velocity does not affect the wound edge geometry.

3.2. Profile of the cost functions

For a given assay, we denote by $(u_{exp}(t, \mathbf{x}))$ the sequence of experimental cell monolayer images, segmented and binarized, and by $(W_{exp}(t))$ the corresponding experimental wound area.

We have considered as cost functions to be minimized the following:

$$\text{Cell density error : } J_U(r, D) = \int_{[T_0, T]} \int_{\Omega} |u(t, \mathbf{x}) - u_{exp}(t, \mathbf{x})|^2 d\mathbf{x} dt \quad (11)$$

$$\text{Wound area error : } J_A(r, D) = \int_{[T_0, T]} |W(t) - W_{exp}(t)|^2 dt \quad (12)$$

where u is the computed solution of the Fisher-KPP equations for a given pair of parameters (r, D) and $W(t) = \int_{\Omega} (1 - u(t, \mathbf{x})) d\mathbf{x}$ is the computed wound area.

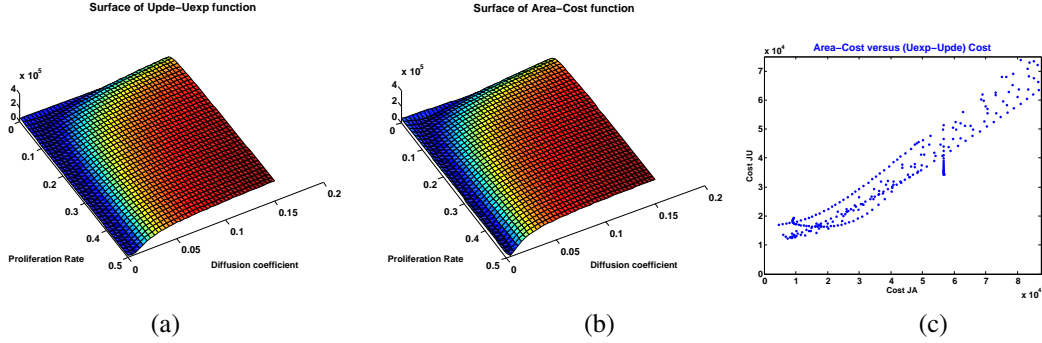


Figure 4: Surface plot of costs (a) J_U and (b) J_A as function of the parameters (r, D) where $r \in [r_{min}, r_{max}]$ and $D \in [D_{min}, D_{max}]$. (c) Image set of $(J_A(r, D), J_U(r, D))$ is plotted for the same set of parameters. The costs show globally some correlated variation. Close to their minima, the relative position of the values located at the image set boundary indicates that indeed they are conflicting.

The cost function J_A is introduced in order to study its relevance to be used as an error-function, that is, its ability to yield correct model parameters at its minimal value.

We performed the computation of the cost functions surfaces for several assays. The results were all similar. We present here one that corresponds to an inhibited migration, a case which illustrates a pathological behaviour of the cost J_A .

A characteristic common to all our studied assays is that the cost surfaces plotted in Figure-4 (a)(b) show that both the minima of J_U and J_A are located at the confluence of extremely flat narrow valleys. Consequently, one has to choose a robust and accurate numerical optimizer. We used the SQP (Sequential Quadratic Programming) algorithm of the 'fmincon' module from Matlab.

We plotted in Figure-4 (c) the profile of $(J_A(r, D), J_U(r, D))$ for a uniform 40×40 sampling of $[r_{min}, r_{max}] \times [D_{min}, D_{max}]$. Globally, the two costs J_A and J_U show some correlated variation; Interestingly, close to their minima, which is the region of interest for our study, these two functions are quite antagonistic. In order to help us answer

the question: which cost function is the most relevant for the parameter identification? we led different studies, essentially numerical because of the intricate implicit relation satisfied by the two functions with respect to the parameters r and D .

Indeed, many authors (see e.g. [26]) assume that the experimentally measured leading edge velocities are close to $V_{th} = 2\sqrt{rD}$, the theoretical velocity of the Fisher-KPP wavefront, and then use the latter to compute the diffusion coefficient D given the cell proliferation rate r (doubling time tables excerpt from published data) through the formula $V_{exp} \approx 2\sqrt{rD}$. So, we found it interesting to investigate the dependance of the considered costs with respect to the difference in velocities $V_{gap} = \frac{V_{exp} - V_{th}}{V_{exp}}$ where V_{exp} is the experimentally measured one using the sequence of binarized images.

The study of the dependence of the wound area cost J_A and cell density one J_U with respect to the parameter V_{gap} led us to the following observations, see Figure-5:

- (i) for all assays, the global minimum of J_A as a function of \sqrt{rD} always occurred at $V_{gap}(r, D) \approx 1$, *id est* at $D = D_{min}$.
- (ii) for inhibited migration assays, the assumption $V_{gap} \approx 0$ was irrelevant to yield the optimal values of the model parameters.

Thus, we abandoned the recourse to the wound area cost function J_A (and convex combination with the cost J_U turned out to be useless), and as well we abandoned the a priori constraining of $V_{gap}(r, D)$ to zero. Remarkably, we nevertheless observed, from our numerical results, that for migration assays, which are neither activated nor inhibited, the approximation $V_{exp} \approx V_{th}$ holds a posteriori, see Table-1 .

4. Results

We performed the assessment of the validity of the F-KPP mathematical model on five MDCK monolayer assays : a reference one, two activated and two inhibited migration conditions. Two different situations are considered, depending on the success or failure of the wound closure.

4.1. Wound closure occurs

In the following, the results of three different MDCK cell-sheet assays are discussed. They have in common that the scraped wound closed. The first one referred to as Assay-I is a reference one, also known as control assay, where no migration activators or inhibitors were used. In the two other assays, Assay-II and Assay-III, HGF (Hepatocyte Growth Factor) a well known migration activator of epithelial cells is added to the control (Assay-I) setting.

For the three assays, we first comment in a few words the profiles computed by exploiting the experimental data, using the segmented and binarized image sequences. Then, we compare the experimental profiles and parameters to the corresponding computed ones.

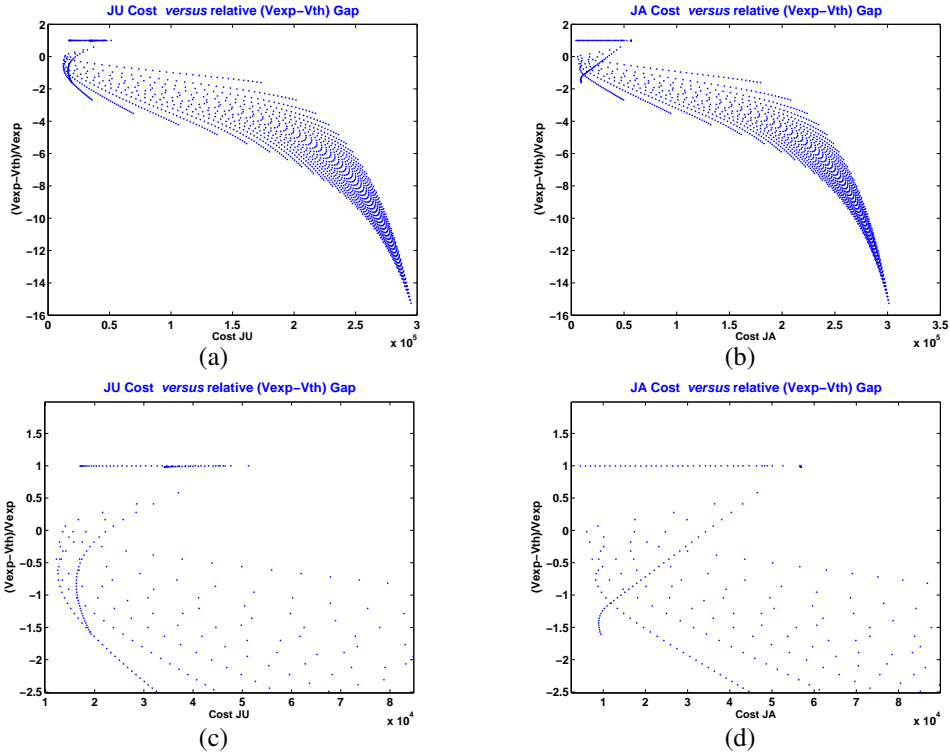


Figure 5: Plot of the image set (J_U, J_A) of costs J_U and J_A with respect to the velocity gap $V_{gap} = \frac{V_{exp} - V_{th}}{V_{exp}}$ for a uniform 40×40 sampling of $[r_{min}, r_{max}] \times [D_{min}, D_{max}]$. (a) (c) Plot of $(J_U(r, D), V_{gap}(r, D))$ and a close view of the "Paradise bird's" head. (b) (d) Plot of $(J_A(r, D), V_{gap}(r, D))$ and a close view of the "Paradise bird's" head. Remark that the segment $V_{gap}(r, D) = 1$ as visible on the top of (d) corresponds to the minimal value $D = D_{min}$.

A reference assay: regular wound closure

We have plotted in Figure-6(a) the evolution of the wound area for a total duration of 120×6 min. The wound closed shortly after 70×6 min. The discontinuity slope of the wound area observed around 40×6 min is due to the segmentation algorithm which performs poorly when the opposite wound edges touch each other at some point.

The discontinuity observed in Figure-6(b) and the peak observed in Figure-6(e) (they occur around $T = 48 \times 6mn$) correspond also to the first contact between wound opposite edges. The edge mean velocity profile in Figure-6(e) is rather constant until the opposite parts of the wound edge enter into contact (until the peak).

Figure-6(d) shows that if one records the time-averaged speed of the pixels located at the wound edge, then some cells (that is, some collection of neighbor pixels) exhibit higher speeds, in more precisely three distinct locations. This observation may have a link with the so-called leader cells, see [17].

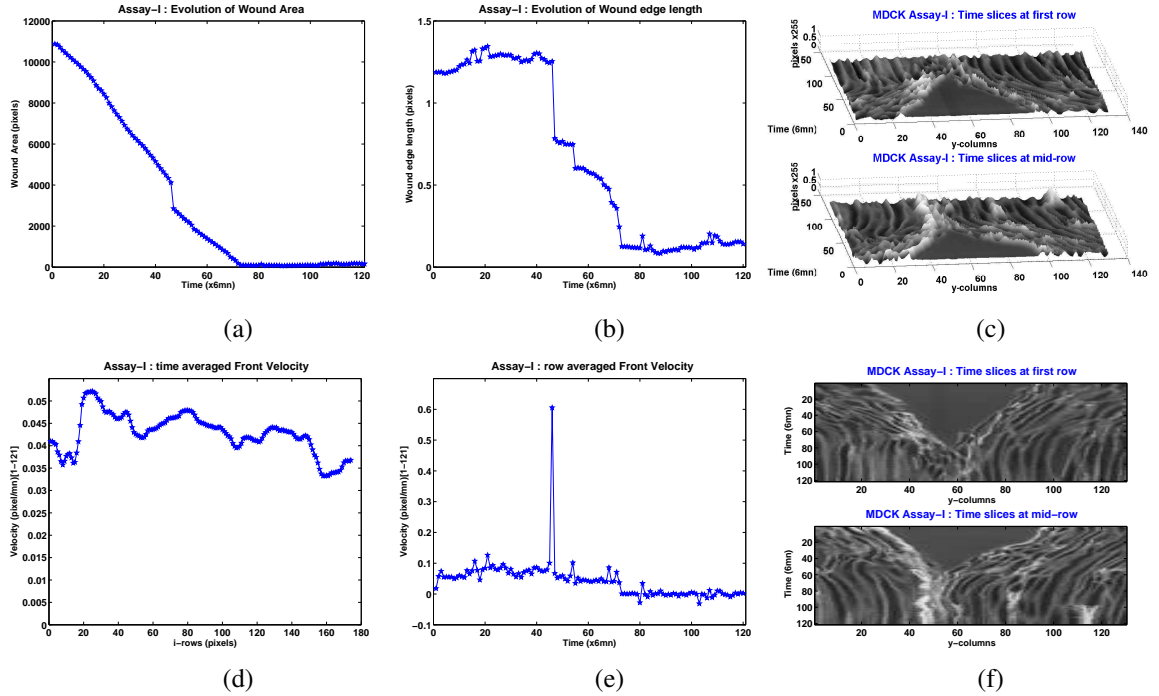


Figure 6: **Assay-I** (a) Time evolution of wound area (in pixel). (b) Time evolution of the leading-edge length (in pixel). (c) 3D XT view at first and mid-rows. (d) Mean (in time) velocity of pixels located at the leading edge (in pixel/min). (e) Averaged (in space) leading-edge velocity (in pixel/min). (f) 2D XT view at first and mid-rows.

In Figure-6(c), we have plotted the XT slices (kymographs) with as 3rd dimension the pixel intensity in order to picture how far the cell-sheet migration is from a pure scattering dynamics. Indeed, without mitosis, apoptosis and maybe some videography defocalization, we would observe lines of continuous smooth ridges. We project the 3D view in a 2D one in Figure-6(f), to get a visual representation of the speed profile for first and mid-range rows of the image sequences.

Assay-I: Computational results compared to experimental data

Table-1 and Figure-7 show a very good accordance between the observed biological parameters and the model predicted ones, notably the Fisher-KPP model accurately predicted total closure time (shortly after 70×6 min).

An activated migration: speedy wound closure

The MDCK monolayer Assay-II corresponds to an HGF activated migration case.

The evolution of the wound area during the closure depicted in Figure-8(a) shows that there are two distinct phases: the first one occurs roughly speaking during the image interval [1-20], and the second one occurs around [20-36] with a larger slope.

V_{exp}	V_{comp}	V_{th}	$MR_{exp}(\pm std)$	$MR_{comp}(\pm std)$	r	D	J	$T_0 - T$
0.0619	0.0668	0.0832	20.35(± 7.77)	20.98(± 7.76)	0.070	2.48E-02	0.02	1-20
0.0722	0.0745	0.0918	23.78(± 8.54)	24.08(± 7.94)	0.056	3.77E-02	0.02	1-30
0.0738	0.0771	0.0902	23.58(± 8.00)	25.00(± 7.69)	0.058	3.52E-02	0.03	1-35
0.0743	0.0770	0.0795	24.26(± 7.22)	25.09(± 6.54)	0.071	2.22E-02	0.03	1-45

Table 1: **Assay-I.** Comparison of experimental and computed velocities and migration rates (plus standard deviations for migration rates) for the optimally calibrated model parameters. Rows correspond to results computed over a dataset subset $[T_0 - T]$ of the total [1-120] images. Refer to section-3.1 for significance of variables and used units.

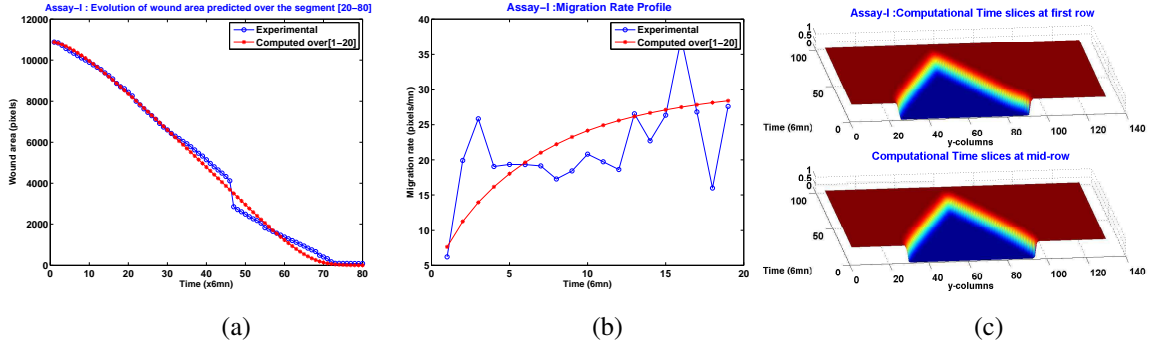


Figure 7: **Assay-I. Computational vs experimental wound evolution.** (a) Time variation of experimental (blue) versus computed (red) wound area (in pixel). (b) Time variation of the experimental (blue-dot) versus computed (red) migration rate (in pixel/min). (c) 3D XT view at first and mid-rows.

The wound edge mean velocity plotted in Figure-8(e) corroborates this distinction, and one may observe that the velocity magnitude is slightly greater than 0.10 during the [20-36] interval, 36 being the image at which opposite edges come into contact.

Compared to the reference assay, the topology of the ridges shown in Figure-8(c) look more hectic, and the 2D projected image Figure-8(f) shows a velocity profile (the contour of the homogeneously grey region) which is not a rectilinear triangle as observed in Figure-6(f).

The total length of the leading edges Figure-8(b) seems to have lower fluctuation than in the reference case, except close to the occurrence of the fronts contact.

The distribution of the mean (time-averaged) front velocity with respect to the pixels location is plotted in Figure-8(d). Cells located at the mid and bottom rows tend to be faster, but no obvious localized leading regions, except the middle, arises from the profile.

Assay-II: Computational results compared to experimental data

Taking into account our remark on the two-phase evolution of the wound area, we have performed two numerical experiments. The first one presented in Figure-9 corresponds to the parameters identified using the image interval [1-20], and the second one shown in Figure-10 uses the larger image interval [1-36].

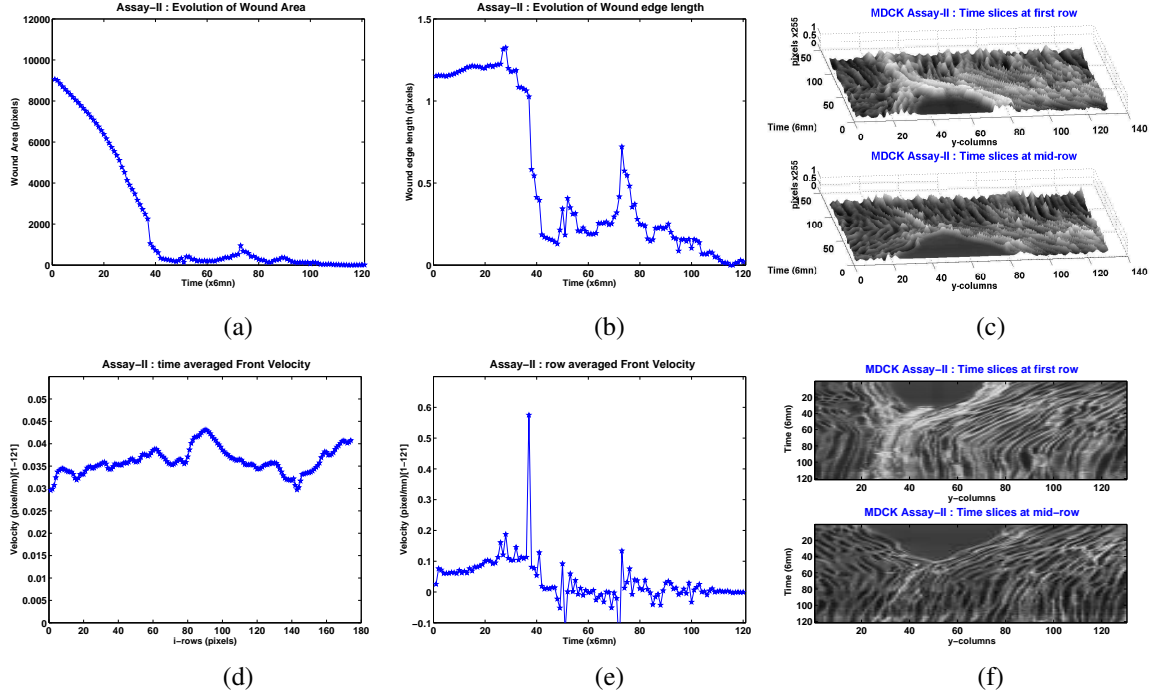


Figure 8: **Assay-II** (a) Time variation of wound area (in pixel). (b) Time variation of the leading-edge length (in pixel). (c) 3D XT view at first and mid-rows. (d) Mean (in time) velocity of pixels located at the leading edge (in pixel/min). (e) Averaged (in space) leading-edge velocity (in pixel/min). (f) 2D XT view at first and mid-rows.

V_{exp}	V_{comp}	V_{th}	$MR_{exp}(\pm std)$	$MR_{comp}(\pm std)$	r	D	J	$T_0 - T$
0.0671	0.0692	0.0471	22.38(± 7.02)	21.92(± 6.36)	0.196	2.83E-03	0.02	1-20
0.0904	0.0916	0.1177	30.43(± 12.06)	29.72(± 9.53)	0.049	7.13E-02	0.03	1-36

Table 2: **Assay-II**. Comparison of experimental and computed velocities and migration rates (plus standard deviations for migration rates) for the optimally calibrated model parameters. Rows correspond to results computed over a dataset subset $[T_0 - T]$ of the overall $[1-120]$ images. Refer to section-3.1 for significance of variables and used units.

The numerical results shown in Table-2 illustrate how critical may be the choice of the fitting experimental dataset. Indeed, since the time evolution of the wound area is no more linear-wise, even experimental velocity and migration rate data are sensitive to the used experimental dataset $[T_0 - T]$.

We observe in Figure-9 that for the first computational experiment using the image interval $[1-20]$, the mathematical model Fisher-KPP is unable to predict the wound evolution beyond the used fitting interval (which is the least one should expect).

Interestingly, the computational area profile does however unstick from the experimental one (see Figure-9(a)), precisely at the initiation of the second faster phase cited above, that is, around image 20. Thus, performing the model-dependent parameter identification using early experimental data may discriminate distinct evolution phases,

in a more easier "visual" way (the unsticking) than could e.g. a first derivative profile which is generally quite noisy.

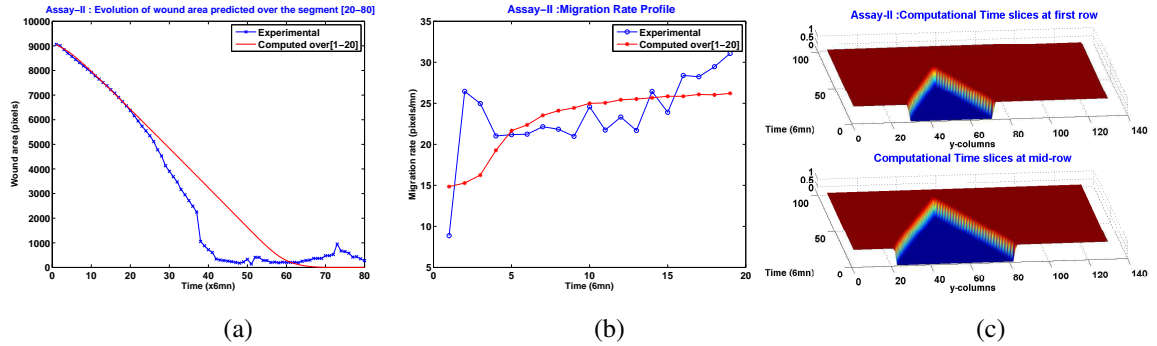


Figure 9: **Assay-II using dataset [1-20] for calibration. Computational vs experimental wound evolution.** (a) Time variation of experimental (blue) versus computed (red) wound area (in pixel). (b) Time variation of the experimental (blue-dot) versus computed (red) migration rate (in pixel/min). (c) 3D XT view at first and mid-rows.

Observe also that in Figure-10(c), the XT slices show a left-right stiff front with monotonic decreasing from 1 to 0 which is drifted by steady translation along the "triangle" edges, while in Figure-9, the triangle sides show some unexpected oscillations. These oscillations seem to be closely related to the small magnitude in diffusion coefficient, see the case-study of Assay-V.

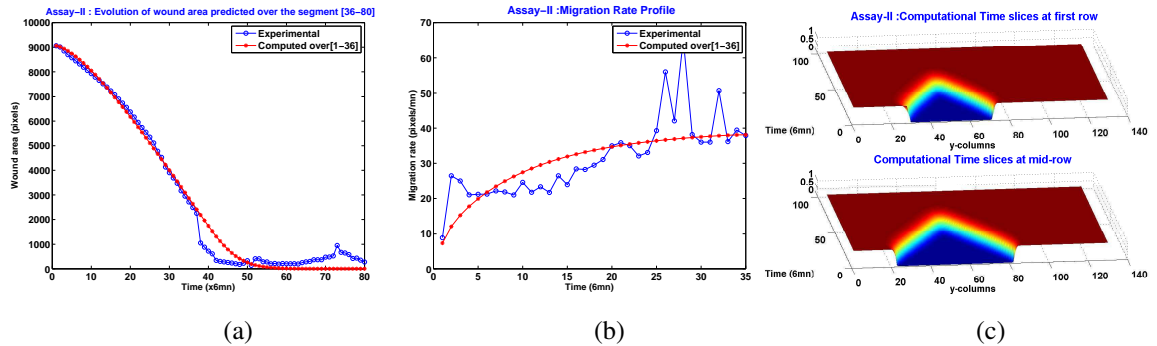


Figure 10: **Assay-II using dataset [1-36] for calibration. Computational vs experimental wound evolution.** (a) Time variation of experimental (blue) versus computed (red) wound area (in pixel). (b) Time variation of the experimental (blue-dot) versus computed (red) migration rate (in pixel/min). (c) 3D XT view at first and mid-rows.

An activated migration: accelerating wound closure

As for Assay-II, in the MDCK cell-sheet Assay-III we have added HGF to the reference conditions.

The Hepatocyte Growth Factor also induced a visible faster wound closure compared to the reference Assay-I, but this assay exhibited remarkably different dynamics compared to the Assay-II.

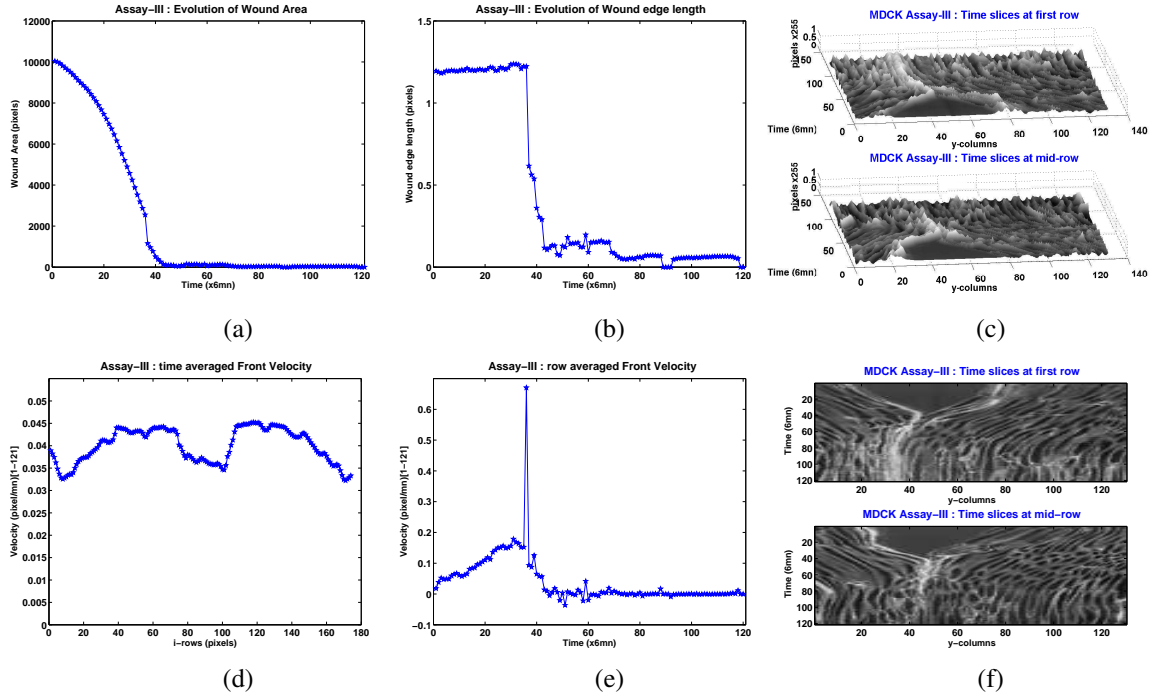


Figure 11: **Assay-III** (a) Time variation of wound area (in pixel). (b) Time variation of the leading-edge length (in pixel). (c) 3D XT view at first and mid-rows. (d) Mean (in time) velocity of pixels located at the leading edge (in pixel/min). (e) Averaged (in space) leading-edge velocity (in pixel/min). (f) 2D XT view at first and mid-rows.

The time evolution of the wound area is clearly nonlinear as can be seen from Figure-11(a) which, comparably to Assay-II, tends to show two different stages, the first one in the range [1-20] and the second one in the range [20-36]. These two regimes are more visible from Figure-12(a) when around image 20 the mathematical model prediction unsticks from the experimental measurements.

However, slightly differently from Assay-II, we observe a much more convincing invariance of the total length of the wound edge during the closure, see Figure-11(b). One also observes a patent accelerating wound front visible from Figure-11(e). Indeed, despite the averaged experimental velocity shown in Table-3, the mean edge velocity during the time interval from 30 to 35 ($\times 6$ min) lies between 0.150 to 0.180 (twice the velocity magnitudes observed in Assay-II).

From Figure-11(d) where is plotted the mean velocity (from initiation to closure) of each row pixel located on the wound edge, we can also observe an important difference with Assay-II. Here, two visible leading regions arise which are disjoint and located at $1/3$ and $2/3$ of the image row width.

The 3D XT view in Figure-11(c) and its 2D projection in Figure-11(f) visually show even more hectic ridges than for the Assay-II, but we did not assess it quantitatively.

Assay-III: Computational results compared to experimental data

We observe that as for Assay-II, and contrarily to the reference Assay-I, the optimal model parameters strongly depend on the portion of data used for the identification process, and also are, but to a lesser extent, the mean velocities and migration rates, as can be seen from Table-3.

V_{exp}	V_{comp}	V_{th}	$MR_{exp}(\pm std)$	$MR_{comp}(\pm std)$	r	D	J	$T_0 - T$
0.0646	0.0648	0.0849	21.55(± 9.01)	20.38(± 7.62)	0.063	2.86E-02	0.02	1-20
0.1028	0.0950	0.1327	34.67(± 16.87)	30.93(± 10.40)	0.036	1.21E-01	0.04	1-36

Table 3: **Assay-III.** Comparison of experimental and computed velocities and migration rates (plus standard deviations for migration rates) for the optimally calibrated model parameters. Rows correspond to results computed over a dataset subset $[T_0 - T]$ of the total $[1-120]$ images. Refer to section-3.1 for significance of variables and used units.

The comparison of experimental versus computational wound areas, as plotted in Figure-12(a), show that the Fisher-KPP model using the optimal parameters sticks on the experiment only during the time used for the calibration. The model is unable to follow the wound area evolution as it enters an accelerated phase. Of course, the latter is all but unexpected, since the Fisher-KPP equation with the logistic growth term cannot behave differently than following with constant velocity the initial front, as tend to show the rectilinear-sided triangles in Figure-12(c).

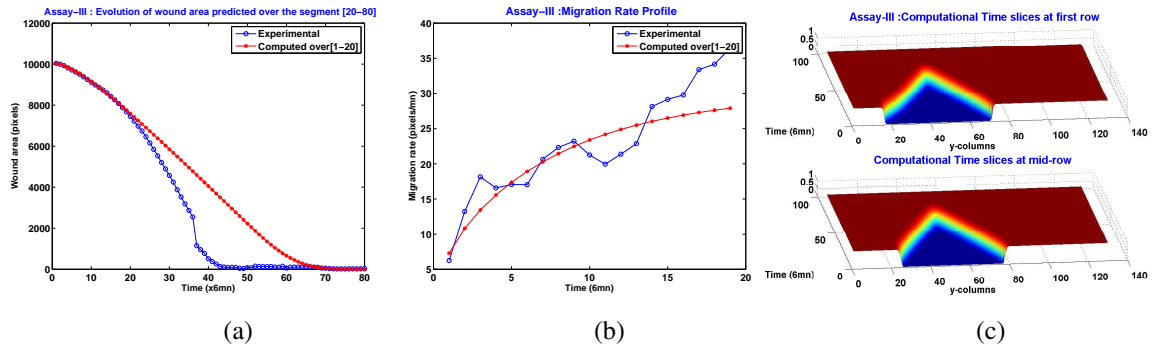


Figure 12: **Assay-III. Computational vs experimental wound evolution.** (a) Time variation of experimental (blue) versus computed (red) wound area (in pixel). (b) Time variation of the experimental (blue-dot) versus computed (red) migration rate (in pixel/min). (c) 3D XT view at first and mid-rows.

4.2. Wound closure fails

We present in this section two assays, Assay-IV and Assay-V, where we added to the control conditions an inhibitor of the cell-sheet migration, the LY 294002 (more precisely, LY29 inhibits PI3-kinase). For the two assays, both experimental and model-computed mean front velocities, migration rates and wound area profiles are to some extent comparable. A noticeable difference lies in the range of the calibrated model parameters. Wound edge mean velocity is, for both Assay-IV and Assay-V, two to five times smaller than the reference assay; but for Assay-IV the diffusion coefficient D is

comparable in order to the reference ones, while it is two to three orders less in the case of Assay-V.

An inhibited migration with a normal diffusion parameter

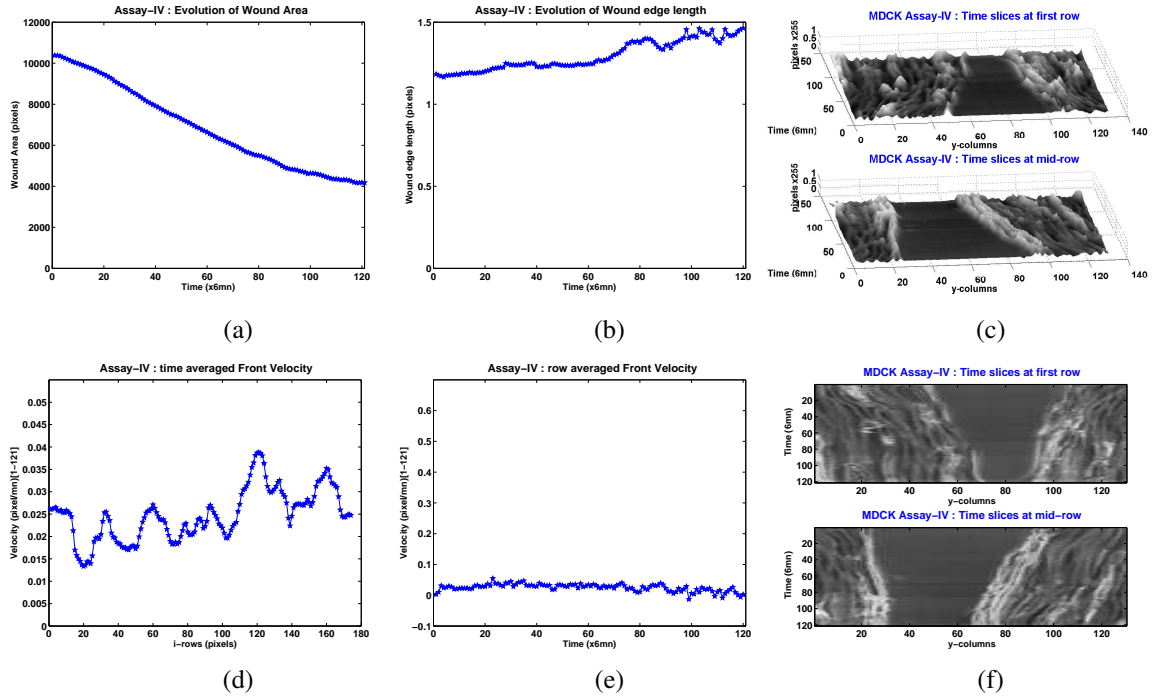


Figure 13: **Assay-IV** (a) Time variation of wound area (in pixel). (b) Time variation of the leading-edge length (in pixel). (c) 3D XT view at first and mid-rows. (d) Mean (in time) velocity of pixels located at the leading edge (in pixel/min). (e) Averaged (in space) leading-edge velocity (in pixel/min). (f) 2D XT view at first and mid-rows.

The wound area depicted in Figure-13(a) first slowly decreases until approximately image 80. Then it enters a stagnation phase during the dataset interval [80-120]. During this interval, the wound velocity is close to zero as shown Figure-13(e).

The profile of the wound front length Figure-13(b) shows an increase in magnitude and in total variation, indicating a possible persistent front cells (lamellipodial) activity.

Assay-IV: Computational results compared to experimental data

From Table-4 we observe that velocities, migration rates and model parameters are more or less half the values of the corresponding reference assay. We show in Figure-14(a) the time variation of the model-computed wound area compared to the experimental one. The model parameters were fitted using only the dataset [1-20], but the model correctly predicts the wound evolution during the interval [20-40] that is for two hours later. The unsticking of the model from the experimental area becomes thereafter increasingly more visible.

V_{exp}	V_{comp}	V_{th}	$MR_{exp}(\pm\text{std})$	$MR_{comp}(\pm\text{std})$	r	D	J	$T_0 - T$
0.0240	0.0250	0.0429	7.76(± 3.07)	7.94(± 3.15)	0.030	1.53E-02	0.01	1-20
0.0313	0.0322	0.0461	10.27(± 3.74)	10.57(± 3.63)	0.025	2.10E-02	0.02	1-40
0.0317	0.0345	0.0406	10.18(± 3.11)	11.34(± 3.18)	0.023	1.76E-02	0.04	1-80

Table 4: **Assay-IV.** Comparison of experimental and computed velocities and migration rates (plus standard deviations for migration rates) for the optimally calibrated model parameters. Rows correspond to results computed over a dataset subset $[T_0 - T]$ of the total [1-120] images. Refer to section-3.1 for significance of variables and used units.

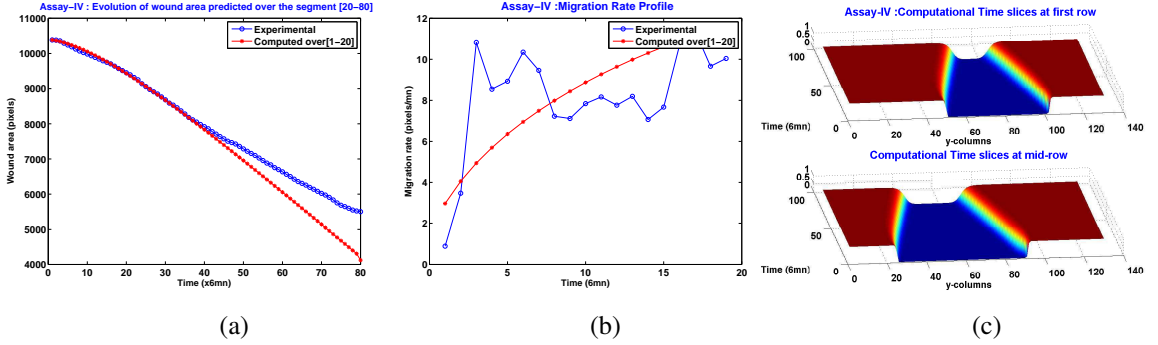


Figure 14: **Assay-IV using dataset [1-20]. Computational vs experimental wound evolution.** (a) Time variation of experimental (blue) versus computed (red) wound area (in pixel). (b) Time variation of the experimental (blue-dot) versus computed (red) migration rate (in pixel/min). (c) 3D XT view at first and mid-rows.

Let us remark that the Fisher-KPP equations used in the present setting to model the wound front progression do not predict anything else than an ineluctable wound closure, be it in short or very long time. So, the use of mathematical models of the Fisher-KPP kind for inhibited migration assays must be carefully handled. We show here and for the next assay, that the Fisher-KPP model is unable to render the whole story, because of the inhibition effect. If a given inhibitor has an effect of only slowing the migration without freezing it at some point, then Fisher-KPP prediction may reveal more efficient than for the present case. As illustrated by Assay-II and Assay-III, the same remark holds as is for the activation case.

An inhibited migration with a small diffusion parameter

The experimental profiles for the inhibited migration Assay-V are shown in Figure-15. Wound area (a) slows during the interval [1-80] then stagnates during the [80-120] time interval. The stagnation is obvious from (e) the mean wound edge velocity profile which vanishes during the latter interval. The length of the leading edge (b) does barely increase in the course of the assay. As for Assay-IV, we observe in (d) localized -roughly speaking, three- leading regions of pixels.

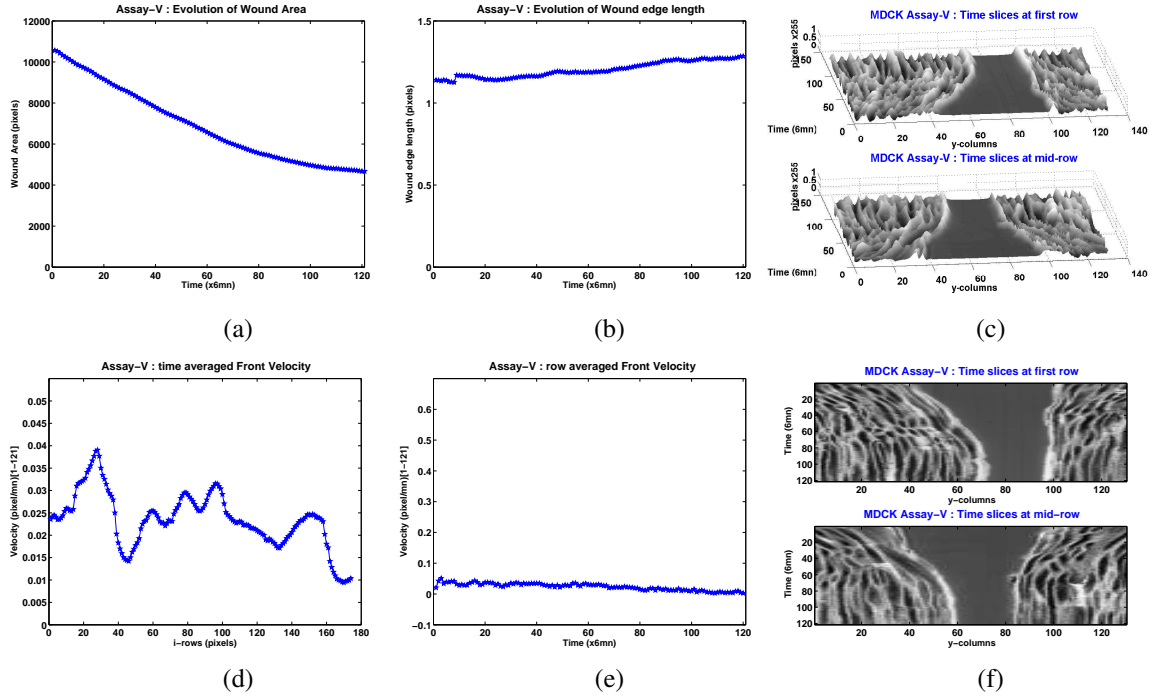


Figure 15: **Assay-V.** (a) Time variation of wound area (in pixel). (b) Time variation of the leading-edge length (in pixel). (c) 3D XT view at first and mid-rows. (d) Mean (in time) velocity of pixels located at the leading edge (in pixel/min). (e) Averaged (in space) leading-edge velocity (in pixel/min). (f) 2D XT view at first and mid-rows.

Assay-V: Computational Results compared to experimental data

The three first rows in Table-5 are the results obtained for the cost $J = J_U$, and the last one is for the wound area cost $J = J_A$. We comment on the last row at the end of the current section. As seen before, the results are very sensitive to the choice of the dataset used for the identification of the model parameters. Contrarily to the reference assay, we observe a critical absence of consistency in the magnitudes of the model parameters, despite the relative consistency of the experimental versus computational mean velocities and migration rates.

The Fisher-KPP model is clearly unable to predict the evolution of the wound area beyond the fitting interval, as shown in Figure-16(a). Moreover, enlarging the fitting dataset from [1-20] to [1-90] does not improve the prediction, compare with Figure-17(a). As already pointed out, the Fisher-KPP model always achieves the wound closure in finite time Figure-17(c). The comparison of the experimental versus computational wound areas show in Figure-17(a) that the diffusion coefficient ($D = 3.7 \cdot 10^{-2}$) identified with the dataset [1-90] is too large, leading to the irrelevant computational early closure.

The fourth row in Table-5 shows a case study with $J = J_A$ as cost function (gap between experimental and model wound areas, averaged with respect to the total duration

V_{exp}	V_{comp}	V_{th}	$MR_{exp}(\pm std)$	$MR_{comp}(\pm std)$	r	D	J	$T_0 - T$
0.0354	0.0381	0.0205	11.69(± 3.65)	12.23(± 3.58)	0.148	7.05E-04	0.01	1-20
0.0337	0.0351	0.0058	11.54(± 2.72)	11.73(± 3.98)	0.231	3.68E-05	0.02	1-40
0.0294	0.0360	0.0486	9.86(± 2.89)	11.86(± 3.59)	0.016	3.74E-02	0.07	1-90
0.0307	0.0330	0.0026	10.43(± 2.50)	11.24(± 4.83)	0.268	6.41E-06	$J_A = 0.05$	1-80

Table 5: **Assay-V**. Comparison of experimental and computed velocities and migration rates (plus standard deviations for migration rates) for the optimally calibrated model parameters. Rows correspond to results computed over a dataset subset $[T_0 - T]$ of the total [1-120] images. The last row, with used dataset [1-80] the used cost is the wound area gap $J = J_A$. Refer to section-3.1 for significance of variables and used units.

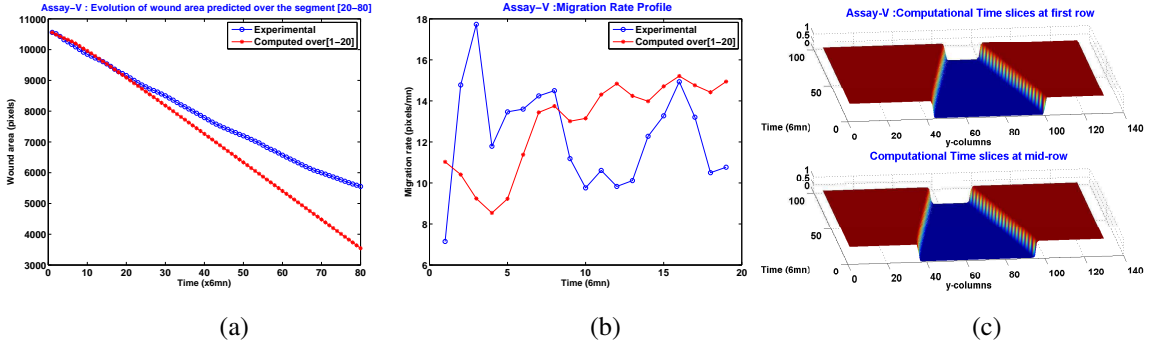


Figure 16: **Assay-V using dataset [1-20]. Computational vs experimental wound evolution.** (a) Time variation of experimental (blue) versus computed (red) wound area (in pixel). (b) Time variation of the experimental (blue-dot) versus computed (red) migration rate (in pixel/min). (c) 3D XT view at first and mid-rows.

of the used dataset). We already mentioned in section 3.2, devoted to a preliminary computational study, that we were not confident in the relevance of the J_A cost as a calibration indicator.

The numerical results are shown in Figure-18. As expected, the profile of the model wound area (a) matches the experimental one clearly better than shown in Figure-16(a) with the cost J_U . But this matching is obtained through quite periodic small oscillations, which seem to constraint the Fisher-KPP solution to behave in a non standard (that is, monotonic) way. The computational migration Figure-18(b) rate shows strong oscillations up and down of the experimental ones. And the 3D XT slices (c) show transversally waving walls. We have paid attention to make sure that these observed oscillations are not due to the classical numerical instability of our explicit Euler scheme. Indeed, the use of refined spatial and temporal step-sizes, as well as implicit Euler, Crank-Nicholson and second order splitting schemes led to the same observations.

The observed oscillating profiles do not exist in our cell-sheet experiments. Indeed, the optimization process yielded a large value for the proliferation rate r and a small value for the diffusion parameter D (notice however that the optimal $D = 6.10^{-6}$ is greater than the minimal bound $D_{min} = 10^{-8}$). We postulate (ongoing work) that, for the Fisher-KPP equations, there is a link between the rising of these oscillations for particular values of the model parameters, namely large enough r and small enough D which result from the minimization of the cost J_A , and the oscillatory behavior ob-

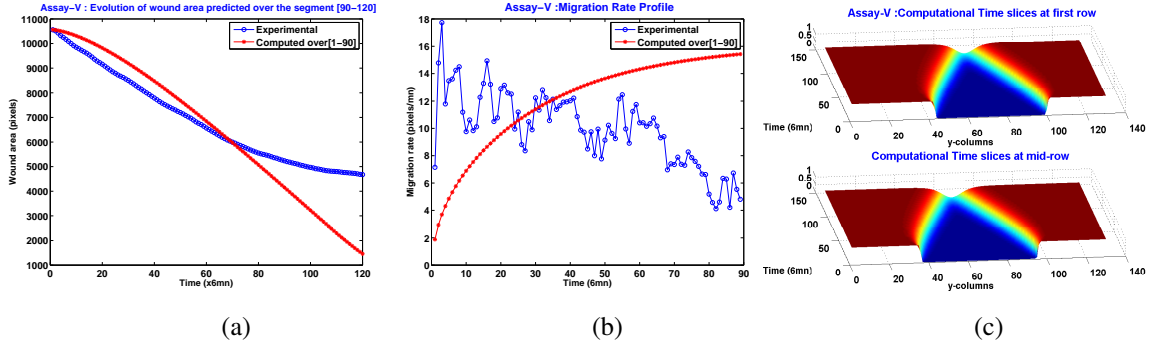


Figure 17: **Assay-V using dataset [1-90]. Computational vs experimental wound evolution.** (a) Time variation of experimental (blue) versus computed (red) wound area (in pixel). (b) Time variation of the experimental (blue-dot) versus computed (red) migration rate (in pixel/min). (c) 3D XT view at first and mid-rows.

served for Fisher-KPP equations with delay terms. We think that some finite difference schemes may mimic such a behavior for a small enough diffusion coefficient.

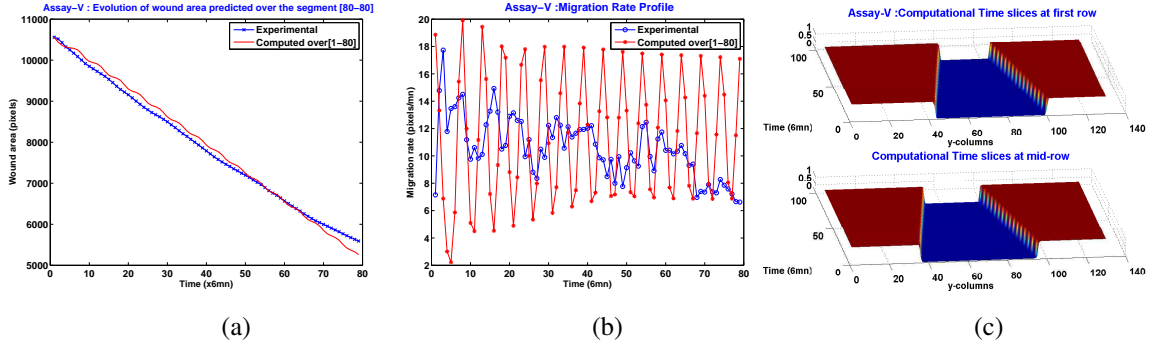


Figure 18: **Assay-V using dataset [1-80] with $J = J_A$. Computational vs experimental wound evolution.** (a) Time variation of experimental (blue) versus computed (red) wound area (in pixel). (b) Time variation of the experimental (blue-dot) versus computed (red) migration rate (in pixel/min). (c) 3D XT view at first and mid-rows.

5. Conclusion

We addressed in this paper the ability of the Fisher-KPP equation, a two-parameter mathematical model, to render some of the dynamical features of epithelial cell-sheets during wound closure. We based our approach on a nonlinear parameter identification formulation, in a two-dimensional setting, and using 2D image processing (segmentation, binarization) of the video acquired sequences. The overall computational machinery was used to study five MDCK monolayer assays in a reference, activated and inhibited migration conditions.

We found that for the reference assays, that is assays where migration was not exogenously activated or inhibited, as several previous works pointed out, the wound

velocity was constant. We also proved that the Fisher-KPP equation was able to accurately predict, until the final closure of the wound, the evolution of the wound area, the mean velocity of the cell front, and the time at which the closure occurred. We observed the consistency of the identified parameters for different choices of the experimental datasets used to feed the identification process. Remarkably, we observed that both the experimental and computational mean velocity of the wound edge were close to the theoretical Fisher-KPP wavefront speed, without imposing it *a priori*.

Afterwards, we found that for activated as well as for inhibited migration assays, many of the cell-sheet dynamics could not be well captured by the mathematical model. Indeed, it is not surprising that accelerating or decelerating wound fronts cannot be well approximated by constant speed fronts. Quantities like as the mean velocity of the wound edge or rate of migration were still relevant and in good accordance with their experimental corresponding data, but the identified model parameters were very sensitive to the dataset used for the calibration process. Though, we may say that the Fisher-KPP model could help us in spotting possibly different regimes of the wound closure, at least when they deviate (unstick) from a regular "Fisher-KPP" one, if we term by such a regime whose evolution is well rendered by the calibrated Fisher-KPP equation.

Let us also stress the role of the Fisher-KPP parameters. Although these two parameters, denoted by r and D are termed the proliferation rate and the diffusion coefficient, careful attention should be paid to their biophysical meaning in the present context. Here, the parameter r barely represents the genuine cell proliferation rate. Even in a rough approximation, the latter should be of the magnitude of the early exponential growth rate, related to the doubling time T_D through the relation $r \approx \ln 2 / T_D$. So, even for the shortest MDCK doubling times found in the literature, around 10 hours, the parameter r should be at least one to two orders below the actually computed optimal values. The diffusion parameter D has to be small enough to preserve the stiffness of a likely initial wound profile, which requirement is in contradiction with the use of too small proliferation rates if one seeks a theoretical or even a numerical front speed close to the experimental one. The theoretical speed $V_{th} = 2\sqrt{rD}$ would be too small compared to the experimental one. Moreover, diffusion coefficients D , even small enough to keep the stiff front propagation, still locally diffuse lamellipodial and filopodial protrusions (thanks to the normal flow generated by the Laplace operator), leading to their early fading in the mathematical simulations, while still present in the biological process. The diffusion parameter accounts for only partially tenable approximation of the complex cell spreading and scattering processes.

Thus, in our opinion, in view of our numerical experiments, the model parameters r and D should be regarded as rather abstract yet discriminating model parameters, which nevertheless yield correct (compared to the experimental ones) migration rate and wound mean velocities. Handled with care, both Fisher-KPP equations and the optimally calibrated parameters may be used for the classification of cell-sheet wound closures.

Finally, our study has shown that the use of error functions based on the difference between experimental versus model-computed wound area may lead to numerical

pathological bias, that is, the apparition of non biological oscillations. To our knowledge, this is the first time such oscillations are observed for the Fisher-KPP classical system, and we consider as a positive byproduct the mathematical challenge posed by the understanding and justification of such behavior.

- [1] A Saez, E Anon, M Ghibaudo, O du Roure, J-M Di Meglio, P Hersen, P Silberzan, A Buguin, and B Ladoux. Traction forces exerted by epithelial cell sheets. *Journal of Physics: Condensed Matter*, 22(19):194119, 2010.
- [2] Gabriel Fenteany, Paul A. Janmey, and Thomas P. Stossel. Signaling pathways and cell mechanics involved in wound closure by epithelia cell sheets. *Current Biology*, 10(14):831–838, 2000.
- [3] Qi Bao and R. Colin Hughes. Galectin-3 and polarized growth within collagen gels of wild-type and ricin-resistant mdck renal epithelial cells. *Glycobiology*, 9(5):489–495, 1999.
- [4] Alexandre Saez, Axel Buguin, Pascal Silberzan, and Benoît Ladoux. Is the mechanical activity of epithelial cells controlled by deformations or forces? *Biophysical Journal*, 89(6):L52 – L54, 2005.
- [5] Sri Ram Krishna Vedula, Man Chun Leong, Tan Lei Lai, Pascal Hersen, Alexandre J. Kabla, Chwee Teck Lim, and Benoît Ladoux. Emerging modes of collective cell migration induced by geometrical constraints. *Proceedings of the National Academy of Sciences*, 109(32):12974–12979, 2012.
- [6] Qinghui Meng, James M. Mason, Debra Porti, Itzhak D. Goldberg, Eliot M. Rosen, and Saijun Fan. Hepatocyte growth factor decreases sensitivity to chemotherapeutic agents and stimulates cell adhesion, invasion, and migration. *Biochemical and Biophysical Research Communications*, 274(3):772–779, 2000.
- [7] Jui-Fen Lai, Shu-Chen Kao, Si-Tse Jiang, Ming-Jer Tang, Po-Chao Chan, and Hong-Chen Chen. Involvement of focal adhesion kinase in hepatocyte growth factor-induced scatter of madin-darby canine kidney cells. *J. Biol. Chem*, 275(11):7474–7480, 2000.
- [8] Esko Kankuri, Dana Cholujova, Monika Comajova, Antti Vaheri, and Jozef Bizik. Induction of hepatocyte growth factor/scatter factor by fibroblast clustering directly promotes tumor cell invasiveness. *Cancer Res*, 65(21):9914–22, November 2005.
- [9] M Delehedde, N Sergeant, M Lyon, P S Rudland, and D G Fernig. Hepatocyte growth factor/scatter factor stimulates migration of rat mammary fibroblasts through both mitogen-activated protein kinase and phosphatidylinositol 3-kinase/akt pathways. *Eur J Biochem*, 268(16):4423–9, August 2001.
- [10] Claire M Wells, Arie Abo, and Anne J Ridley. Pak4 is activated via pi3k in hgf-stimulated epithelial cells. *J Cell Sci*, 115(Pt 20):3947–56, October 2002.

- [11] Mao Ye, Danning Hu, Lili Tu, Xiangtian Zhou, Fan Lu, Bin Wen, Wencan Wu, Yi Lin, Zhonglou Zhou, and Jia Qu. Involvement of pi3k/akt signaling pathway in hepatocyte growth factor-induced migration of uveal melanoma cells. *Invest Ophthalmol Vis Sci*, 49(2):497–504, February 2008.
- [12] J Moss and M Vaughan. Molecules in the arf orbit. *J Biol Chem*, 273(34):21431–4, August 1998.
- [13] Julien Viaud, Mahel Zeghouf, H el ene Barelli, Jean-Christophe Zeeh, Andr e Padilla, Bernard Guibert, Pierre Chardin, Catherine A. Royer, Jacqueline Cherfils, and Alain Chavanieu. Structure-based discovery of an inhibitor of arf activation by sec7 domains through targeting of protein-protein complexes. *Proceedings of the National Academy of Sciences*, 104(25):10370–10375, 2007.
- [14] Anne L Pollack, Gerard Apodaca, and Keith E Mostov. Hepatocyte growth factor induces mdck cell morphogenesis without causing loss of tight junction functional integrity. *Am J Physiol Cell Physiol*, 286(3), March 2004.
- [15] Luis Almeida, Patrizia Bagnerini, Abderrahmane Habbal, St ephane Noselli, and Fanny Serman. A Mathematical Model for Dorsal Closure. *Journal of Theoretical Biology*, 268(1):105–119, January 2011.
- [16] Rizwan Farooqui and Gabriel Fenteany. Multiple rows of cells behind an epithelial wound edge extend cryptic lamellipodia to collectively drive cell-sheet movement. *Journal of Cell Science*, 118(Pt 1):51–63, 2005.
- [17] M. Poujade, E. Grasland-Mongrain, A. Hertzog, J. Jouanneau, P. Chavrier, B. Ladoux, A. Buguin, and P. Silberzan. Collective migration of an epithelial monolayer in response to a model wound. *Proceedings of the National Academy of Sciences*, 104(41):15988–15993, 2007.
- [18] Eamonn A. Gaffney, Philip K. Maini, Jonathan A. Sherratt, and Paul D. Dale. Wound healing in the corneal epithelium: Biological mechanisms and mathematical models. *J. Theor. Med.*, 1(1):13–23, 1997.
- [19] Luke Olsen, Philip K. Maini, and Jonathan A. Sherratt. Spatially varying equilibria of mechanical models: Application to dermal wound contraction. *Math. Biosci.*, 147(1):113–129, 1998.
- [20] P.K. Maini, L. Olsen, and J.A. Sherratt. Mathematical models for cell-matrix interactions during dermal wound healing. *Int. J. Bifurcation Chaos Appl. Sci. Eng.*, 12(9):2021–2029, 2002.
- [21] Karen M. Page, Philip K. Maini, and Nicholas A.M. Monk. Complex pattern formation in reaction-diffusion systems with spatially varying parameters. *Physica D*, 202(1-2):95–115, 2005.
- [22] P. Lee and CW. Wolgemuth. Crawling cells can close wounds without purse strings or signaling. *PLoS Computational Biology*, 7(3):e1002007, March 2011.

- [23] J. A. Fozard, H. M. Byrne, O. E. Jensen, and J. R. King. Continuum approximations of individual-based models for epithelial monolayers. *Mathematical Medicine and Biology*, 27(1):39–74, 2010.
- [24] Nestor Sepulveda, Laurence Petitjean, Olivier Cochet, Erwan Grasland-Mongrain, Pascal Silberzan, and Vincent Hakim. Collective cell motion in an epithelial sheet can be quantitatively described by a stochastic interacting particle model. *PLoS Comput Biol*, 9(3), 2013.
- [25] Alexandre J Kabla. Collective cell migration: leadership, invasion and segregation. *J R Soc Interface*, 9(77):3268–78, December 2012.
- [26] P.K. Maini, D.L.S. McElwain, and D. Leavesley. Traveling waves in a wound healing assay. *Appl. Math. Lett.*, 17(5):575–580, 2004.
- [27] P.K. Maini, D.L.S. McElwain, and D. Leavesley. Traveling wave model to interpret a wound-healing cell migration assay for human peritoneal mesothelial cells. *Tissue Eng.*, 10(3-4):475–482, 2004.
- [28] Julia C. Arciero, Qi Mi, Maria F. Branca, David J. Hackam, and David Swigon. Continuum model of collective cell migration in wound healing and colony expansion. *Biophysical Journal*, 100(3):535 – 543, 2011.
- [29] Anna Q. Cai, Kerry A. Landman, and Barry D. Hughes. Multi-scale modeling of a wound-healing cell migration assay. *Journal of Theoretical Biology*, 245(3):576 – 594, 2007.
- [30] Bram G Sengers, Colin P Please, and Richard O.C Oreffo. Experimental characterization and computational modelling of two-dimensional cell spreading for skeletal regeneration. *Journal of The Royal Society Interface*, 4(17):1107–1117, 2007.
- [31] Matthew J. Simpson, Katrina K. Treloar, Benjamin J. Binder, Parvathi Haridas, Kerry J. Manton, David I. Leavesley, D. L. Sean McElwain, and Ruth E. Baker. Quantifying the roles of cell motility and cell proliferation in a circular barrier assay. *Journal of The Royal Society Interface*, 10(82), 2013.
- [32] Grégoire Malandain and Eric Bardin. Intensity compensation within series of images. In Randy E. Ellis and Terry M. Peters, editors, *Medical image computing and computer-assisted intervention (MICCAI 2003)*, volume 2879 of LNCS, pages 41–49, Montreal, Canada, November 2003. Springer Verlag.
- [33] J. Serra. *Image analysis and mathematical morphology*. Academic Press, London, 1982.
- [34] T.Y. Kong and A. Rosenfeld. Digital topology: introduction and survey. *Computer Vision, Graphics, and Image Processing*, 48(3):357–393, 1989.
- [35] R.A. Fisher. The wave of advance of advantageous genes. *Annals of Eugenics*, 7(4):355–369, 1937.

- [36] A. Kolmogoroff, I. Petrovsky, and N. Piscounoff. Étude de l'équation de la diffusion avec croissance de la quantité de matière et son application à un problème biologique. *Bull. Univ. Etat Moscou, Ser. Int., Sect. A, Math. et Méc. 1*, Fasc. 6:1–25, 1937.
- [37] J.-L. Lions. *Optimal control of systems governed by partial differential equations*. Translated from the French by S. K. Mitter. Die Grundlehren der mathematischen Wissenschaften, Band 170. Springer-Verlag, New York, 1971.